ARCHIVES OF MECHANICS
Arch. Mech. **78** (2), 107–143, 2026, https://doi.org/10.24423/aom.4846

Mechanics of isotropic points under frictional contacts: experimental and theoretical studies

K. V. N. SURENDRA[1)], S. J. ANTONY[2,*)]

[1)] *Department of Mechanical Engineering, Indian Institute of Technology, Palakkad, Kerala, India*

[2)] *School of Chemical and Process Engineering, Faculty of Engineering and Physical Sciences, University of Leeds, UK, e-mail[*)]: S.J.Antony@leeds.ac.uk (corresponding author)*

Understanding the mechanical behaviour of isotropic points (IPs)—regions of hydrostatic stress with zero shear—is essential for interpreting photoelastic fringe patterns and analysing load transfer in solid bodies. This study investigates IP formation and evolution in circular disks subjected to four-point loading using a combination of photoelastic experiments, digital image processing, and analytical modelling. A generalised stress framework based on superposition is developed to predict isochromatic fringe fields and IP locations for arbitrary combinations of normal and tangential contact forces. Beyond case-specific solutions, the study establishes a unified physical interpretation of fringe patterns based on the concepts of zero-shear loci, symmetry constraints, and stress-topology transitions. It is shown that symmetry governs the localisation of IPs along principal axes, while symmetry breaking leads to their migration into the disk interior. Under normal loading, IPs form along boundary-induced zero-shear regions and undergo coalescence and splitting, indicating transitions in stress topology. In contrast, tangential loading produces a persistent central isotropic point corresponding to a null stress state, resulting in qualitatively different fringe evolution. A novel inverse methodology is proposed to determine contact force components from experimentally measured IP coordinates. The results demonstrate that IP locations are invariant to the load magnitude but highly sensitive to the load direction, making them reliable indicators of the load geometry. The findings highlight isotropic points as fundamental descriptors of stress redistribution and fringe topology. While the present study focuses on a circular disk under four-point loading, the framework may be extended to more complex systems such as granular assemblies and contact-driven structures, subject to further investigation.

Key words: isochromatics, isotropic point, circular disk, stress distribution, asymmetric loading, contact friction.

1. Introduction

A photoelastic experiment on a loaded 2-D specimen can reveal two types of fringes: isochromatics and isoclinics. An isochromatic is a locus of constant difference between in-plane principal stresses, while an isoclinic is a locus of constant principal direction within the plane. The zeroth order fringe (ZOF) is one of the isochromatics, where the in-plane principal stresses are equal, which does not change its position with a proportional change in magnitudes of loads (without changing loading direction/s). An isotropic point (IP) is a special case of ZOF forming locally around a point instead of spreading over a curve. An IP is defined as the point through which isoclinics of all orders pass [6–8]. Isotropic points (IPs) are the points of localised hydrostatic state of stress. When a transparent birefringent material is viewed under a polariscope using a white light source, isotropic points appear as dark spots within a colourful fringe pattern. These points help engineers analyse stress distribution, identify areas of minimal shear stress, and detect potential structural weaknesses. They often occur at low shear stress regions and play a crucial role in interpreting photoelastic fringe patterns. By studying isotropic points, engineers can improve material design, optimise structural integrity, and prevent failures in mechanical and civil engineering applications. Information on the evolution of IP points in materials helps to identify regions of redundant materials for their safe removal in applications such as compliant mechanisms [1]. Understandings of their evolution under different loading conditions and geometrical arrangements are vital especially in the applications of design optimisations of materials and structures [2] and material processes involving the fragmentation of granular materials [3–5]. Unlike previous studies that focus on symmetric loading or qualitative fringe analysis, this work presents a closed-form analytical framework for asymmetric loading and validates it experimentally.

In photoelasticity, the plane polariscope and circular polariscope arrangements facilitate the visualisation of isoclinics and isochromatic fringe patterns [6]. Under the plane polariscope arrangement, isotropic points (IPs) refer to the locations within a stressed birefringent material (sample) through which all isoclinics pass. The circular polariscope arrangement, on the other hand, enables the identification of stress concentration zones, typically manifested as higher-order isochromatic fringe accumulation in high-load bearing areas, while low-stress regions exhibit a spread of zeroth-order fringe (ZOF) patterns across a broader area. In certain stress distributions, these low-stress zones are isolated from high-stress zones, a phenomenon that can be revealed through the identification of IPs. The isochromatic fringe field is locally axisymmetric around an IP. The formation of IPs in a solid domain depends on the geometry of the material and the loading configuration. However, the locations of IPs in a loaded body are independent of factors such as the magnitude of a reference load, the photoelastic material's fringe constant, and its thickness.

The concept of IPs was first introduced by Coker and Filon [7], who referred to them as neutral points in their pioneering work. However, we use the term IP in this paper following the later uses. Frocht [8] and Timoshenko and

Goodier [9] demonstrated various examples of IP formation, including beam-related problems. Kuske and Robertson [10] developed a model of the generic 2-D Cartesian stress tensor around an IP for any configuration, using quadratic polynomials to describe isoclinics and isochromatics. Hutchinson *et al.* [11] further modeled the stress tensor around an IP to classify these points. Durelli and Shukla [12] explored fringe topologies around IPs, focusing on free boundaries and corners. Ramesh [13] contributed to the advancement of digital photoelasticity, particularly in automating fringe tracking and counting, including IP identification [14]. Surendra and Simha [15] investigated fringe topologies around IPs in 3-, 4-, and 6-point axisymmetric normal loadings on a circular disk.

Photoelasticity is a whole-field method that enables the measurement of stress states at points of interest and within frictional contacts between two solids. Early work by Uemura *et al.* [16, 17] applied photoelasticity to determine friction coefficients at contact points by measuring traction components. Fedorchenko *et al.* [18] quantified contact normal and shear stresses on die walls in powder compaction using photoelasticity. Comninou [19] employed the analytical Mellin transform and experimental isochromatic patterns to derive the singularity points arising during rough slip of a wedge on a half-plane, which causes friction. Shukla and Nigam [20] introduced a photoelastic experimental-numerical method to determine the Hertzian contact area, normal stresses, and shear (frictional) stresses at contact points from full-field isochromatic data on a three-point loading system of disks. Hariprasad and Ramesh [21] discussed a method to evaluate contact parameters by processing the isochromatics obtained through reflection photoelasticity. Recently, Fernández [22] overcame metrological challenges in photoelastic contact stress quantification and demonstrated the use of generalised least squares with Lagrange multipliers [23]. Barbat and Rao [24] analyzed the contact between a photoelastic sapphire die and the workpiece in a strip drawing operation through isochromatic and isoclinic patterns formed in the die.

Dally and Chen [25] used photoelastic isochromatics to identify friction components at the asperities of a transparent sheet in sliding contact with an adjacent structure, utilising local bending of patterns near the contacts for identification. Burguete and Patterson [26] demonstrated the existence and control of friction between a cylinder and half-space through stress freezing in photoelasticity. Nam *et al.* [27] and Shin *et al.* [28] developed a photoelastic hybrid method for contact stresses in O-rings under diametrical compression and a three-point loading system. They observed a few IPs in the experimental isochromatic patterns of large strain squeezed disks [27, 28]. Recently, Foust *et al.* [29, 30] applied photoelasticity to measure traction at the boundary of bolted joints and thermal stresses in disks under diametric compression.

In recent times, the application of photoelasticity has gained attention in understanding stress distribution within the grain scale in particulate processes. This includes analysing the distribution of maximum shear stress and the direction of principal stresses in grains surrounded by contiguous grains (including asymmetrically loaded grains) and powders under mechanical loading [31–33]. Understanding the shear stress state of grains is crucial for comprehending the breakage properties of granular materials in processing environments [3–5].

Guan *et al.* [34] presented a theoretical approach to quantify the friction repose angle in relation to the inclination of asperities in contacting bodies, such as rigid or elastic granular assemblies. Force transmission chains [4] in such assemblages can be readily identified using photoelastic experiments, where the identification of contact load parameters between two disks is essential. Surendra and Simha [35] evaluated the coefficient of friction using IP coordinates in a circular disk under four-point loading symmetric about two perpendicular diameters, as shown in Fig. 1(c). Due to the symmetry about two axes, the four contacts are equivalent, and a single value for the static friction coefficient suffices. If symmetry about one axis is disrupted, friction at two independent contacts must be quantified. In the most general case of completely asymmetric four-point loading, as shown in Fig. 1(b), all four contacts need to be analysed independently, as considered in this paper.

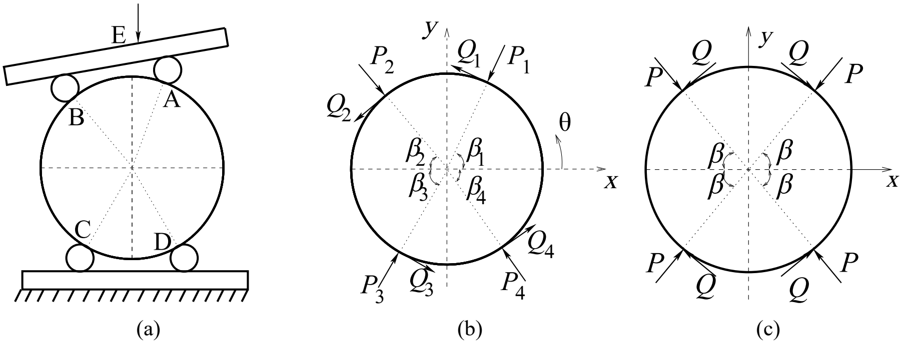

Fig. 1. (a) Schematic of loading setup of the disk specimen in the photoelastic experiment with contact points labelled; (b) free-body diagram of disk specimen; (c) special case of bi-symmetry [35].

Inspired by the fact that IPs can reveal information about far-field contact loading [35], our objective is to determine the normal and tangential components of the four-point contact load applied asymmetrically on circular disks. Rather than solely focusing on friction quantification [34], we also seek to understand the evolution of IP formation patterns in various scenarios and capture them in the closed-form for selected cases. This is accomplished through an analysis that starts with symmetric and/or pure normal/tangential load cases, followed by more general loading environments. The studies presented here are based on a combination of photoelastic experiments and theoretical solutions.

The proposed inverse method for determining contact loads from isotropic point (IP) locations is significant because IPs represent regions of hydrostatic stress with zero shear, which remain invariant to load magnitude and material properties, although they drift due to change in direction of at least one load. This invariance makes IPs reliable markers for stress distribution under complex loading. By linking IP coordinates to contact forces through equilibrium and stress-optic laws, the method enables non-invasive load estimation and provides insight into load transfer mechanisms. Although demonstrated on a circular disk under four-point loading, the approach is broadly applicable in principle to other geometries and loading configurations, although such extensions are not explicitly demonstrated in the present work. This provides a foundation for potential applications in structural optimisation and reverse engineering. However, extension of the present framework to more complex systems such as granular assemblies or bolted joints requires further investigation and validation.

2. Photoelastic experiments

The self-weight of the photoelastic specimen used in the experiment is negligible compared to the applied forces. Thus, specimen weight is ignored in the modelling and analysis. All the problems in this study are analysed within the framework of 2-D linear elasticity under isothermal conditions, assuming homogeneous and isotropic material properties [9]. However, the solutions are applicable to specimens of any thickness, including the limiting cases of plane stress and plane strain, provided that the forces are uniformly distributed along the thickness direction.

All contact forces are modelled as concentrated loads, despite being distributed over a small width within the plane of disk (they are distributed along thickness direction in any case) in practical experiments. Otherwise, the typical stress distribution between a flat plate and a convex surface, as considered in this study, follows the Hertzian contact theory [36]. Since the analysis is based on the locations of isotropic points (IPs), which form sufficiently far from the loading contacts, the point load approximation is justified according to St. Venant's principle.

A circular polariscope arrangement [6, 8] is used to capture experimental isochromatic fringe patterns in the loaded disk specimen. This setup consists of two quarter-wave plates positioned on either side of the loaded specimen, along with a polarizer, analyser, and a light source, as illustrated in Fig. 2. The light source can be either monochromatic or white light. A monochromatic light source produces only dark and bright fringes (binary patterns) in a coarse sense, although subtle variations in intensity can be observed. In contrast, a white

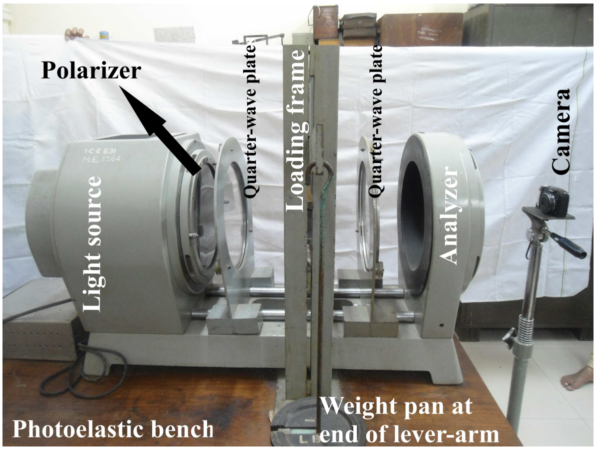

Fig. 2. Circular polariscope used for the experiment, viewed normal to the axis of polariscope from the right side.

light source, which consists of multiple wavelengths, generates a spectrum of colours forming fringe patterns. To achieve a dark-field background, the polariser and analyser axes are crossed (oriented perpendicular to each other within their planes). Under this configuration, using a monochromatic light source, dark fringes formed in a stressed specimen correspond to integer fringe orders $(0, 1, 2, \ldots)$, which can be quantitatively analysed in experiments.

2.1. Fabrication

The required specimens were fabricated by cold casting a large sheet of 6 mm thickness using Epoxy Resin, which was hardened with Triethylene Tetramine in a 100 : 9 weight ratio. The mixture was allowed to cure completely over two days, resulting in a transparent solid sheet. Circular specimens with a diameter of 60 mm were then cut from the fully solidified sheet, as shown in Fig. 3.

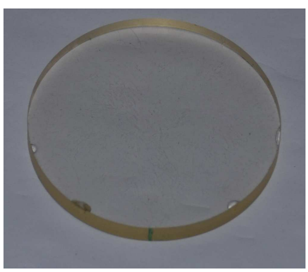

Fig. 3. Typical epoxy resin specimen: circular disk of 6 cm diameter.

2.2. Calibration for material fringe constant

Isochromatic fringes are defined as loci of constant values of difference of *in-plane* principal stresses, i.e., they are contours of distribution of $\sigma_1-\sigma_2$ in the loaded disk region. Here, σ_1 and σ_2 are the in-plane major and minor principal stresses, respectively. The stress optic law leads to the following relation between the state of stress, material and optical properties [6, 8]:

$$\sigma_1-\sigma_2=\frac{Nf_\sigma}{h}, \tag{2.1}$$

where h is the thickness of the specimen, which is 6 mm here; f_σ is the material fringe constant measured in N/m-fringe, which depends on the type of specimen material and N is the fringe order at the point of interest. The isochromatic fringes appear as non-intersecting patterns within the specimen. A fringe of any order may manifest as a curve segment, a closed curve, or isolated points. The latter case of isolated points is theoretical for higher order fringes, and practical for ZOF. When forming as a curve (either open or closed), its width varies along its span due to the gradient of the fringe field. In cases where the fringe appears as a point-type feature, it spreads over a small circular region with gradually diminishing intensity from the center. The size of this region depends on the fringe gradient [8].

A Zeroth Order Fringe (ZOF) that forms as a point is referred to as an Isotropic Point (IP), at which the fringe field is locally axisymmetric. All isoclinics pass through an IP. An isoclinic represents the locus of constant in-plane principal stress direction and is superimposed on the isochromatic pattern when a plane polariscope arrangement is used. A different isoclinic appears when the relative orientation of the polarizer with respect to analyzer is altered. Since IPs carry crucial mechanical information about the stress distribution and contact mechanics, they are the primary focus of this work.

For the determination of f_σ, the classical problem of a circular calibration disk under diametral compression is selected, as its analytical stress distribution solution is well established by Hertz [6, 8]. In brief, the centre of the disk is chosen as the calibration point, where the principal stress difference due to diametral compression by point loads is related to f_σ using stress-optic law as [6, 8]:

$$f_\sigma=\frac{4P}{\pi R N_{\text{centre}}}=\frac{4}{\pi R}\left(\frac{P}{N_{\text{centre}}}\right), \tag{2.2}$$

where P is the magnitude of applied load and R is disk radius. Since, f_σ and R are constants for a given specimen, the relation between applied load (P) and the central fringe order (N_{centre}) is linear. If the fringe order at the centre of the disk (N_{centre}) is measured from the fringe field corresponding to a known external load level, the value of f_σ can be determined. However, instead of relying on a single measurement, multiple N_{centre} values are recorded for different applied loads, and f_σ is obtained from the slope of a straight-line fit between N_{centre} and the applied load P. In the present study, the value of f_σ for the samples used is found to be 12058 N/m. Alternative methods exist for determining the stress-optic coefficient, such as those used for float glass [37].

2.3. Asymmetric four-point loading experiment

A horizontal rigid bar with cylindrical pins welded on one side, as shown in Fig. 4, is fixed to the frame of the polariscope. This bar is positioned at the bottom of the disk to provide two-point loads through reaction forces. Another similar loading bar is placed at the top, but unlike the bottom bar, it remains unconstrained. To introduce asymmetry in the loading, the top bar is inclined. A vertical force is applied to the top face of this bar through a fixed protrusion of the loading arm, which is then transmitted to the disk via two contact points between the pins and the disk periphery. Consequently, the top bar remains in equilibrium due to the combined effect of the two reaction forces at the pins and the applied top load.

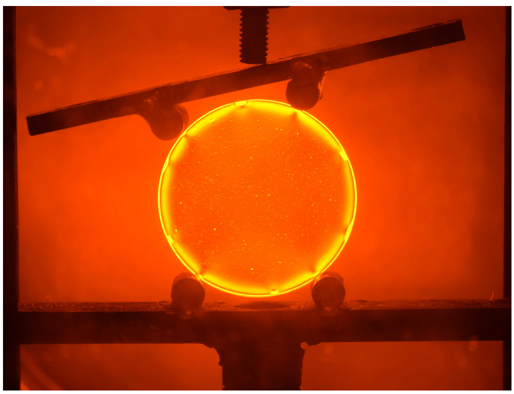

Fig. 4. Loading fixture arrangement for four-point loading of the disk specimen in a circular polariscope setup.

Figure 4 illustrates the bright-field isochromatic fringe pattern of a disk specimen corresponding to a negligible (near-zero) load at the top. The bright-field background is achieved by aligning the axes of polarization for the polarizer and analyser parallel to each other. This setup is initially used to clearly distinguish the loading/support bars from the specimen in the photoelastic image. For the main experiment, where the required isochromatic pattern is analysed, the dark-field configuration of the circular polariscope is used [6, 8].

The load is applied in gradual increments to the four-point constrained disk using a lever-arm mechanism attached to the photoelastic bench, as shown in Fig. 2. Dark-field isochromatic fringes are captured using both monochromatic and white light sources under an external load of 790 N and are presented in Fig. 5. As expected, the experimental isochromatic fringe pattern does not exhibit any symmetry. Two isotropic points (IPs) are identified, each enclosed by a locally '8'-shaped first-order fringe ($N = 1$), which also envelops the four load points, as marked in Fig. 5(a). Higher-order fringes are concentrated only at the four loaded points on the disk periphery. The independent coordinates of each IP provide critical information for determining the normal and tangential load components at the four contact points. This establishes a direct link between IP formation and the mechanical load transfer characteristics in the asymmetrically loaded disk.

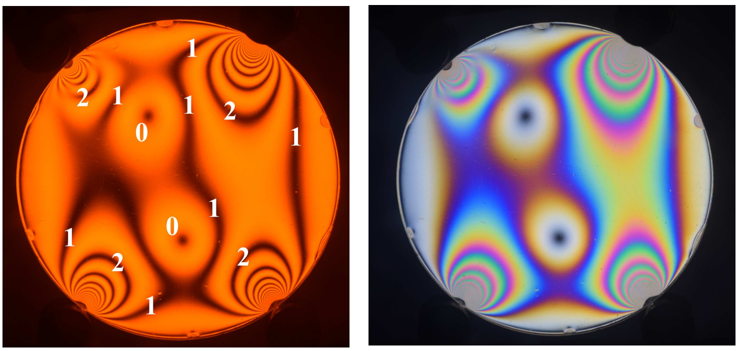

(a) (b)

Fig. 5. Photoelastic experimental isochromatic patterns corresponding to the top load of 790 N under: (a) monochromatic light (N values or fringe orders marked), (b) white light.

2.4. Digital image analysis of the isochromatics

To identify the coordinates of isotropic points (IPs) and load points (Fig. 5(b)), photoelastic images captured under a white light were processed using the digital image analysis. The zeroth-order fringe (ZOF), appearing as black spots, was used to locate IPs. The disk diameter was calibrated to convert pixel measurements into physical coordinates (Fig. 6), enabling accurate mapping of IP and load point positions. These coordinates were subsequently used in the analytical framework for determining contact loads (Section 5).

The disk diameter is measured to be 2078 px (pixels) horizontally and 2047 px vertically. The slight difference between these measurements is attributed to the small asymmetric deformation of the disk under compressive loading. To ensure

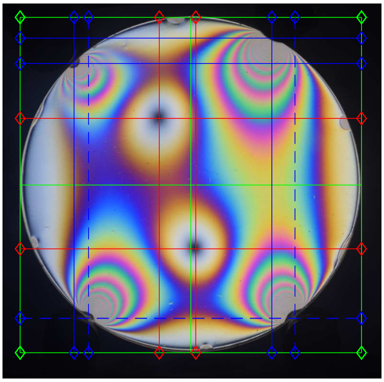

FIG. 6. Coordinate lines marked on a typical digital image for referencing the IPs and load points. Red lines pass through IPs; blue lines through load points.

accuracy in subsequent calculations, the higher value of 2078 px is adopted as the reference diameter. This choice is based on the assumption that the applied load only marginally reduces the disk's vertical dimension, while the horizontal measurement remains a more reliable representation of the original diameter. Meter per pixel can now be obtained as (0.06 m)/(2078 px) = 28.87×10^{-6} m/px. This conversion factor is used to map the digital coordinates of the required points in the image to their corresponding physical coordinates.

The following convention is used here: positive x-axis points towards right horizontally, positive y-axis pointing vertically upwards, origin at the disk centre and the digital x and y coordinates of IP_1 (forming in the upper half of disk) and IP_2 (forming in the lower half) are measured as $(x_{\mathrm{IP}1}, y_{\mathrm{IP}1}) = (-192, 406.5)$ px and $(x_{\mathrm{IP}2}, y_{\mathrm{IP}2}) = (30, -389.5)$ px, respectively. The actual polar coordinates can be obtained using meter per pixel and Cartesian to polar conversions, as: $(r_{\mathrm{IP}1}, \theta_{\mathrm{IP}1}) = (0.4327R, 115.3^\circ)$ and $(r_{\mathrm{IP}2}, \theta_{\mathrm{IP}2}) = (0.376R, -85.6^\circ)$, where R is the disk radius (= 0.03 m). Similarly, angular positions of load points on the periphery are measured as: $\theta_1 = 61.2^\circ$, $\theta_2 = 133.8^\circ$, $\theta_3 = -127.4^\circ$ and $\theta_4 = -52.1^\circ$, all measured from +ve x-axis with counter-clockwise (CCW) direction as +ve. Referring to Fig. 1, and using the above θ_i values measured, the following values are obtained: $\beta_1^{\mathrm{exp}} = 61.2^\circ$, $\beta_2^{\mathrm{exp}} = 46.2^\circ$, $\beta_3^{\mathrm{exp}} = 52.6^\circ$ and $\beta_4^{\mathrm{exp}} = 52.1^\circ$. Note the closeness of β_3 and β_4 as they should be equal theoretically due to the horizontal placement of the bottom loading bar, which has symmetrical geometry. These parameters serve as input for determining the load components at the four contacts on the disk in Section 5.

With regard to the error propagation, the digital image analysis used for determining the coordinates of isotropic points (IPs) and load angles involves minor uncertainties arising from pixel resolution, calibration, and semi-automated identification of feature locations. These uncertainties propagate through the analytical framework by introducing perturbations in the spatial coordinates of IPs. However, this propagation remains bounded for two key reasons. First, IP locations correspond to zeroth-order fringe (ZOF) conditions, which are inherently less sensitive to intensity gradients compared to higher-order fringes, leading to more stable localisation. Second, the inverse formulation developed (Section 5) results in a system of linear equations in the unknown load components, thereby mitigating amplification effects that are typically associated with high-order polynomial sensitivity. Consequently, small errors in pixel-based measurements translate into proportionally small variations in the recovered load components. The close agreement between experimental and analytically reconstructed fringe patterns (e.g., presented later in Fig. 18) supports the robustness of the proposed methodology against such uncertainties.

3. Rigid body analysis

To determine the actual loads applied on the disk, we need to identify the parameters involved and the constraints imposed on individual parts of the loading system. According to Fig. 1(b), there are 12 parameters: 4 normal loads (P_1, P_2, P_3, P_4), 4 tangential loads (Q_1, Q_2, Q_3, Q_4) and 4 angular positions on the disk boundary $(\beta_1, \beta_2, \beta_3, \beta_4)$ for a given disk specimen. The four angular positions are fixed in a given experiment, which are known in this case from the digital image analysis described in Section 2.4.

The rigid body static analysis of the disk leads to certain constraints, which form the set of equations for determining contact loads presented later in Section 5. Referring to Fig. 1(b), the equilibrium of the disk in horizontal, vertical (force components) and θ (in-plane moment) directions, leads to:

$$\begin{aligned}
&\sum F_x = 0 \Rightarrow -P_1 \cos\beta_1 + P_2 \cos\beta_2 + P_3 \cos\beta_3 - P_4 \cos\beta_4 \\
&\qquad\qquad - Q_1 \sin\beta_1 - Q_2 \sin\beta_2 + Q_3 \sin\beta_3 + Q_4 \sin\beta_4 = 0, \\
&\sum F_y = 0 \Rightarrow -P_1 \sin\beta_1 - P_2 \sin\beta_2 + P_3 \sin\beta_3 + P_4 \sin\beta_4 \\
&\qquad\qquad + Q_1 \cos\beta_1 - Q_2 \cos\beta_2 - Q_3 \cos\beta_3 + Q_4 \cos\beta_4 = 0, \\
&\sum M_{\text{DiskCenter}} = 0 \Rightarrow R(Q_1 + Q_2 + Q_3 + Q_4) = 0.
\end{aligned} \tag{3.1}$$

In addition to the above presented three equations, the vertical load transferred through the loading points at the top is given by the following equation:

$$- P_1 \sin\beta_1 - P_2 \sin\beta_2 + Q_1 \cos\beta_1 - Q_2 \cos\beta_2 = -P, \tag{3.2}$$

where P is the magnitude of vertical load transferred from the top-loading bar of the lever-arm mechanism, and $-$ve sign pertains to its downward direction.

4. Analytical prediction of the isotropic points

The state of stress in a circular disk under four-point oblique loading can be derived using the method presented in Appendix A. The stress tensor solution is given by:

$$
\begin{aligned}
[\sigma] &= \sum_{i=1}^{4} [\sigma]^{\mathrm{GenFl}}(P = P_i,\, \gamma = 0,\, \alpha = c_i + (-1)^i \beta_i) \\
&\quad + \sum_{i=1}^{4} [\sigma]^{\mathrm{GenFl}}(P = Q_i,\, \gamma = -90^\circ,\, \alpha = c_i + (-1)^i \beta_i) \\
&\quad + \frac{\sum_{i=1}^{4} P_i}{2\pi R h} \begin{bmatrix} 1 & 0 \\ 0 & 1 \end{bmatrix},
\end{aligned}
\tag{4.1}
$$

in which 9 tensors are added including the last tensor for hydrostatic stress. The first summation includes four tensors corresponding to 4 normal loads and the second summation of four tensors corresponding to tangential loads. In Eq. (4.1), $c_i = 90^\circ$ for $i = 1, 4$ and $c_i = -90^\circ$ for $i = 2, 3$.

The simulated photoelastic isochromatic fringe order (N) can be obtained by substituting the in-plane stress components of Eq. (4.1) into the stress-optic law Eq. (2.1), which can be re-written as follows:

$$
N(r, \theta) = \frac{h}{f_\sigma} \sqrt{[\sigma_{rr}(r, \theta) - \sigma_{\theta\theta}(r, \theta)]^2 + [2\tau_{r\theta}]^2}. \tag{4.2}
$$

From Eq. (4.2), N is an even function of $[\sigma_{rr}(r, \theta) - \sigma_{\theta\theta}(r, \theta)]$ and $\tau_{r\theta}(r, \theta)$. This implies that the isochromatic fringe field is invariant with loading reversal leading to a change in the sign of all the stress components. At ZOF particularly IPs, $N = 0$, which implies:

$$
\begin{aligned}
\sigma_{rr}(r_{\mathrm{IP}}, \theta_{\mathrm{IP}}) &= \sigma_{\theta\theta}(r_{\mathrm{IP}}, \theta_{\mathrm{IP}}), \\
\tau_{r\theta}(r_{\mathrm{IP}}, \theta_{\mathrm{IP}}) &= 0,
\end{aligned}
\tag{4.3}
$$

which provide two independent equations (in general non-linear) in two unknown coordinates of an IP.

While multiple loading configurations are analysed in the following subsections, the resulting isochromatic fringe patterns and isotropic point (IP) behaviour can be understood through a small set of governing physical mechanisms. These include the role of symmetry in defining zero-shear loci, the influence of load type (normal versus tangential), and the evolution of IPs through formation, coalescence, and migration. Each of the following cases is therefore interpreted within this unified framework.

4.1. Normal loading symmetric about an axis

To understand the patterns of IPs formation, initially, we consider the scenario of symmetric normal loading with respect to the x-axis but asymmetric about the y-axis, as shown in Fig. 7. First of Eqs. (3.1) for this special case leads to:

$$P_1 \cos \beta_1 = P_2 \cos \beta_2, \tag{4.4}$$

whereas the other two lead to identities owing to the symmetry of the problem. Because of Eq. (4.4), only two parameters (β_1 and β_2) can be varied independently as one of the loads is known from the applied reference load.

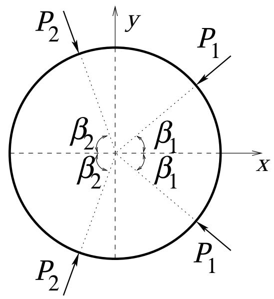

Fig. 7. Circular disk under four-point normal loading symmetric about only the x-axis and asymmetric about the y-axis.

This special case is solved for stresses using Eq. (4.1) considering that $Q_i = 0$ for all i and $P_3 = P_2$, $P_4 = P_1$. The distributions of the two normal stress components, obtained from the stress tensor solution, and the fringe order (Eq. (4.2)) exhibit symmetry about the x-axis. In contrast, the shear stress component exhibits anti-symmetry about the x-axis, indicating that the x-axis serves as a zero-shear axis. From a physical standpoint, symmetry about the x-axis enforces the shear stress component to vanish along this axis, making it a natural zero-shear locus. Since isotropic points correspond to zero-shear states, they are therefore constrained to lie initially on the symmetry axis. Isochromatic patterns are simulated for this special case by varying β_2 between and $90°$ for a given value of β_1. Ten videos are generated corresponding to $\beta_1 = 0°, 10°, \ldots, 90°$ using MATLAB. Three videos corresponding to $\beta_1 = 10°$, $30°$ and $60°$ are provided as supplementary material as Video 1, Video 2 and Video 3. A few snapshots of the videos are shown in Fig. 8. The evolution of IPs observed in these patterns reflects three fundamental mechanisms: (i) formation of IP pairs along the zero-shear axis, (ii) coalescence of these IPs at a critical loading configuration, and (iii) subsequent migration into the interior of the disk.

In order to explain the procedure to arrive at the simulated isochromatic patterns shown in Fig. 8 or supplementary Videos 1, 2 and 3: consider expression of $N(r,\theta)$ (not given here as unwieldy) obtained by substituting stress component expressions into Eq. (4.2), applicable for the symmetric normal loading, derived using Eq. (4.1) or Appendix A. These expressions for stresses and N form the required analytical solution for further plotting and are functions of the domain coordinates (r,θ). Contour command of MATLAB can plot several loci of $(\sigma_1 - \sigma_2) = c$ or equivalently $N = c$, by assigning several values of constant c. One contour plot generated using MATLAB program can lead to one isochromatic pattern shown in, for example, Fig. 8(a). Many contour plot figures, generated consecutively using a 'for' loop in the corresponding MATLAB program, are stored as individual frames of a video file. As the frames per second (= 18 for the videos of this paper) rate is sufficiently high, we humans feel a continuity of the frames without being able to identify the discrete nature of the frames. The MATLAB program coded (filename: *Cir4N_xaxisSym.m*) for Videos 1–3 is provided as a supplementary material of this article. In the same way, all the further figures and videos are obtained, presented in the later subsections.

The three rows of Fig. 8 show the snapshots from the videos of $\beta_1 = 10°$, $30°$ and $60°$, respectively, as representative cases. The middle column patterns in this figure illustrate the coalescence of IPs, thus single IP appears on the symmetry axis. The first column patterns show the cases of IP pair forming on the x-axis. In the last column patterns, the two IPs form inside the quadrants. MATLAB software is used for generating all the patterns and videos. In all the simulations including the ones shown in later sections, the geometric and other constants input to the MATLAB coding are: $R = 0.03$ m, $h = 0.006$ m and $f_\sigma = 12058$ N/m. The reference load in this case is: $P_1 = 790$ N.

The videos reveal that, in all cases of β_1, a pair of IPs forms on the x-axis for a range of β_2 to coalesce into one IP at a particular β_2 and immediately split into two traversing into quadrants of the disk for the rest of the range of β_2. In all cases, the left IP starts when $\beta_2 = 0°$ from the leftmost point of the boundary $(x, y) = (-R, 0)$, and moves towards the other IP before coalescence. The coalescence of two IPs into a single point represents a transition in the topology of the stress field, where two distinct zero-shear regions merge into one. Beyond this point, symmetry no longer fully constrains the stress field, leading to migration of the IPs into the disk interior. After coalescence, they split into two IPs moving into the quadrants as mirror images about the x-axis, and finally merging into the loading points at the right when $\beta_2 = 90°$. For a given β_1, value of β_2 for which IPs coalesce versus x-coordinate of the merged IP is plotted later as coalescence curve in Fig. 9 and the corresponding equation is provided below in Section 4.1.1.

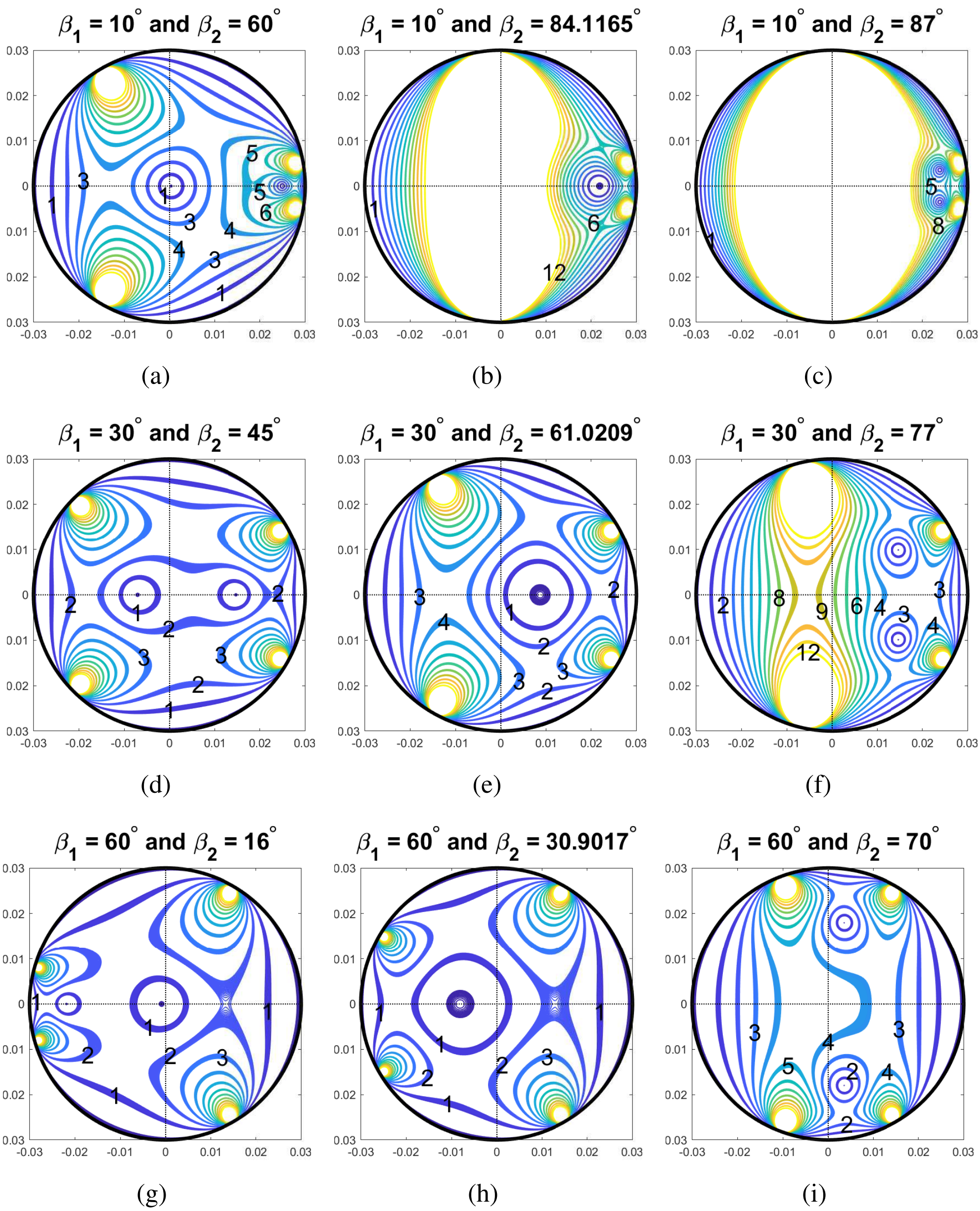

Fig. 8. Simulated isochromatic patterns in circular disk under four-point normal loading symmetric about x-axis for various combinations of β_1 and β_2. Fringe orders (N values) are marked. (a), (b), (c): Video1_Cir4NxaxisBe1_10a.mpg;
(d), (e), (f): Video2_Cir4NxaxisBe1_30a.mpg;
(g), (h), (i): Video3_Cir4NxaxisBe1_60a.mpg.

4.1.1. Tracing of IPs. The exact coordinates of the Isotropic Points (IPs) when they form on the symmetry axis can be determined by solving the first of Eqs. (4.3), specialised along the x-axis. This equation simplifies since, on the symmetry axis, the shear stress component is identically zero

$$\sigma_{rr}(r_{\mathrm{IP}}, 0^\circ) = \sigma_{\theta\theta}(r_{\mathrm{IP}}, 0^\circ), \tag{4.5}$$

where r_{IP} can be replaced by x_{IP} as $\theta = 0^\circ$ on this axis, and the normal stress components are part of the stress tensor solution for this special case of loading. After performing the necessary substitutions and simplifications, the following quartic equation is obtained, characterising the coordinates of the Isotropic Points (IPs):

$$A\left(\frac{x_{\mathrm{IP}}}{R}\right)^4 + B\left(\frac{x_{\mathrm{IP}}}{R}\right)^3 + 2G\left(\frac{x_{\mathrm{IP}}}{R}\right)^2 + B\left(\frac{x_{\mathrm{IP}}}{R}\right) + A = 0, \tag{4.6}$$

where

$$\begin{aligned} A &= 1 - 2\cos\beta_1\cos\beta_2, \\ B &= 4\cos\beta_2 - \cos\beta_1(5 - 2\cos\beta_1\cos\beta_2 + \cos 2\beta_2), \\ G &= (3 + \cos 2\beta_1 - 4\cos\beta_1\cos\beta_2 + \cos 2\beta_2). \end{aligned} \tag{4.7}$$

Note that the polynomial in Eq. (4.6) is symmetric implying that if x is a root then $1/x$ is also a root. The quartic equation is solved using MATHEMATICA software to give the following four roots in terms of normalized x-coordinates of IPs:

$$\frac{x_{\mathrm{IP}}}{R} = \frac{1}{4A}\Big[F + D \pm \sqrt{2F(F+D) - 8A(A+G)}\Big], \tag{4.8}$$

where

$$\begin{aligned} F &= \cos\beta_1(5 + \cos 2\beta_2 - 2\cos^2\beta_1\cos\beta_2 - 4\cos\beta_2), \\ C &= 6\cos\beta_1\cos\beta_2 + \cos\beta_1\cos 3\beta_2 + \cos 3\beta_1\cos\beta_2 \\ &\qquad + 6\cos 2\beta_1 + 6\cos 2\beta_2 - 2\cos 2\beta_1\cos 2\beta_2 - 2, \\ D &= \pm\sqrt{\cos\beta_1\cos\beta_2 C}. \end{aligned} \tag{4.9}$$

The $\pm$ sign in front of the square root in Eq. (4.8), along with the corresponding sign in the expression for D in Eq. (4.9), results in four possible solutions for x_{IP}. These solutions can be categorised as follows:

1) Two physically relevant solutions – These correspond to the actual coordinates of the Isotropic Points (IPs) forming within the disk region.

2) Two hypothetical solutions – These are the reciprocals of the first two roots and correspond to hypothetical IPs that would exist outside the physical boundary of the disk.

Since the experimental and analytical results confirm that IPs always form within the disk, only the first two roots are physically meaningful. Thus, the transition from real roots to complex conjugate roots corresponds physically to the migration of isotropic points from the symmetry axis into the two-dimensional interior of the disk. This provides a direct correspondence between the algebraic structure of the solution and observable fringe behaviour.

During the simplification of Eq. (4.5), after making the required substitutions by dividing by $(r_{\text{IP}}^2 - R^2)$ the quartic equation is arrived at as presented in Eq. (4.6). This step reveals two more roots: $r_{\text{IP}} = \pm R$. These latter roots reflect the fact that the zeroth-order fringe (ZOF) forms continuously along the disk boundary for any combination of β_1 and β_2. This phenomenon arises because the special loading case under consideration falls within the category of pure normal loading, where ZOF always appears along the boundary.

When the roots in Eq. (4.8) are evaluated for a given β_1 value by systematically varying β_2 from zero onward, they initially yield four distinct real roots up to a critical β_2 value, beyond which the roots become complex. After analysing this trend for multiple β_1 values, the following conclusions are drawn:

1) Real Roots and IP Formation on the x-axis
   a) For a given β_1, as long as the roots remain real, two of them satisfy the condition $-1 < x_{\text{IP}}/R < 1$, representing the actual Isotropic Points (IPs) forming on the x-axis.
   b) The other two real roots correspond to hypothetical IPs located outside the physical disk region.
2) Critical β_{2c} and Coalescence of IPs
   a) At a particular β_2 value, denoted β_{2c}, the two real IP roots converge to a single value, indicating the coalescence of the two IPs on the x-axis.
   b) This critical β_{2c} depends on the given β_1 value.
3) Complex Roots and IP Migration into Quadrants
   a) Beyond β_{2c}, the roots transition into complex conjugate pairs:
      i) One pair has an absolute value less than one, representing IPs inside the disk.
      ii) The other pair has an absolute value greater than one, corresponding to hypothetical IPs outside the disk.

b) The real and imaginary parts of the first complex root pair correspond to the x- and y-coordinates of the two IPs, which now migrate into the quadrants, forming mirror images about the x-axis.

4) Verification with Isochromatic Simulations

a) The above findings were rigorously verified for multiple combinations of β_1 and β_2, using visual analysis of simulated isochromatic patterns and video animations.

b) These simulations confirmed that the roots of Eq. (4.8) fully describe the coordinates of IPs for any given β_1 and β_2 in the four-point normal loading case symmetric about the x-axis.

A given root out of four in Eq. (4.8) does not play a unique role such as the left IP coordinate or upper IP coordinates for the complete range of parameters. Equivalently, the four expressions in Eq. (4.8) interchange their roles at different combinations of parameter values. The combinations of β_1 and β_2 at which IPs coalesce are governed by $C = 0$ which makes $D = 0$ which in turn reduces the number of distinct roots to two: one of them is the common normalized x-coordinate of required merged IPs and the other one (reciprocal of first one) is that of merged hypothetical IPs. The four roots are plotted against β_2 within the range of x_{IP}/R: -1 to $+1$ excluding hypothetical IPs range, to capture the locations of the two IPs when they form on the x-axis, as shown in Fig. 9. For a given β_1 value, we can find two curves (top and bottom) meeting when

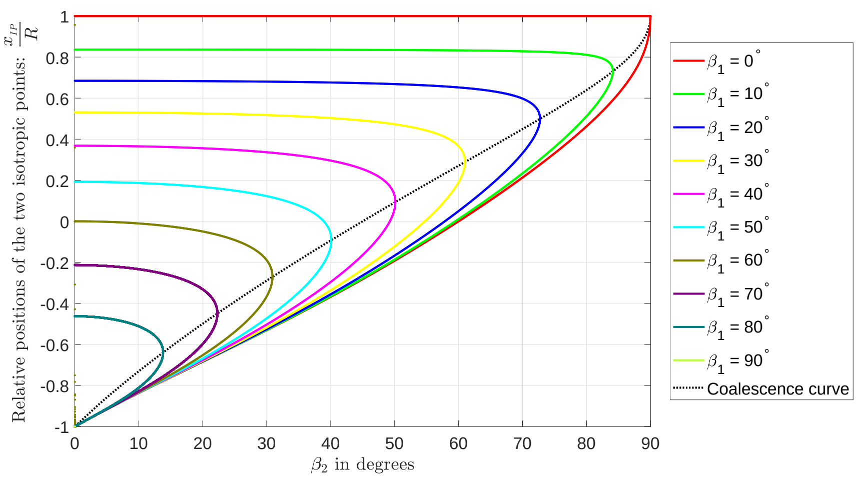

Fig. 9. Normalized radial (or x-) coordinates of pair of isotropic points in circular disk under four-point normal loading symmetric about the x-axis and asymmetric about the y-axis, as β_2 varies for the given β_1 values; when the pair forms on the symmetry axis before coalescence.

$\beta_2 = \beta_{2c}$. The roots are plotted for discrete values of $\beta_1 = 0°, 10°, \ldots, 90°$, representing the motion of two IPs until they coalesce.

Note the smooth convergence of the two curves in each pair shown in Fig. 9, where the meeting points represent the coalescence of IP pairs. In the extreme case of $\beta_1 = 0°$, the setup reduces to a three-point loading case, where the right IP always merges into the boundary ZOF. As a result, only the left IP traverses to the right throughout the corresponding video. This explains why the top pink curve, representing the right IP, remains a horizontal line at $r_{\mathrm{IP}} = R$ for the entire range of β_2. On the other hand, the extreme case of $\beta_1 = 90°$ corresponds to a two-point loading case or diametral compression, where $P_2 = 0$ or no horizontal component of P_1 exists to maintain equilibrium. In this scenario, both IPs merge into the boundary ZOF for all β_2 values, meaning no IPs appear throughout the corresponding video. Consequently, β_2 has no effect in this extreme case, and no curves appear in Fig. 9 for $\beta_1 = 90°$ for the reasons outlined above. For $\beta_2 > \beta_{2c}$, the roots become complex conjugates, whose real and imaginary components correspond to the (x, y) coordinates of the IPs, as established in our previous findings. Leveraging this information, the paths of symmetric IP pairs for different β_1 values are plotted within the disk domain, as shown in Fig. 10. In this figure, the IP trajectories for $\beta_1 = 0°$, $10°$, ..., $90°$ are superimposed, illustrating the behaviour of IPs after their coalescence and subsequent movement away from the x-axis.

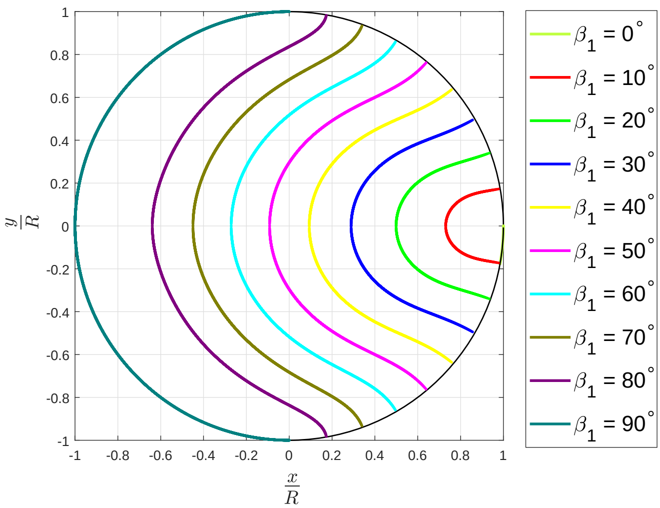

Fig. 10. Paths of pairs of isotropic points in the circular disk under four-point normal loading symmetric about the x-axis and asymmetric about the y-axis, as β_2 varies for the given β_1 values; after splitting.

In Fig. 10, the same colour and line type are used for both IPs in a symmetric pair corresponding to a given β_1. From the figure, the split IPs follow a curved trajectory, starting from their coalescence point on the x-axis and moving towards the loading points (where P_1 acts) on the right. The paths for different β_1 remain parallel, but their spacing is non-uniform, despite β_1 varying uniformly. For the extreme case of $\beta_1 = 0°$ (three-point loading), no curves appear, as the left IP moves along the x-axis, while the right IP remains embedded in the boundary ZOF for the entire β_2 range. In contrast, the semi-circular path shown for $\beta_1 = 90°$ (another extreme case, corresponding to diametric compression) is hypothetical, as no IPs appear throughout this case.

4.1.2. Normal loading symmetric about both the axes. When $\beta_1 = \beta_2 = \beta$ in Fig. 7, the four-point normal loading becomes symmetrical about both x- and y-axes leaving only one parameter to vary. This special case was analysed in SURENDRA and SIMHA [35], in which the IP pair traverses on the x-axis when $0° \le \beta \le 45°$ and on the y-axis when $45° \le \beta \le 90°$. The characteristic equation for IP coordinates given by Eq. (4.6) reduces to the following bi-quadratic equation, in this case:

$$-\cos 2\beta\left(\frac{x_{\mathrm{IP}}}{R}\right)^4 + 2\left(\frac{x_{\mathrm{IP}}}{R}\right)^2 - \cos 2\beta = 0, \tag{4.10}$$

for which the four roots are given by:

$$\frac{x_{\mathrm{IP}}}{R} = \pm\sqrt{\frac{\cos\beta - \sin\beta}{\cos\beta + \sin\beta}},\ \pm\sqrt{\frac{\cos\beta + \sin\beta}{\cos\beta - \sin\beta}}, \tag{4.11}$$

in which the first two roots are coordinates of IPs inside the disk and the last two (reciprocals of the first two) are those of hypothetical IPs. The roots give real values for $0° \le \beta \le 45°$ and purely imaginary values for $45° \le \beta \le 90°$.

In this case, symmetry about both axes further constrains the stress field such that zero-shear conditions exist along both principal directions. As a result, isotropic points remain confined to the symmetry axes, demonstrating the dominant role of symmetry in localising stress features.

4.1.3. Three-point symmetric loading and diametric compression. The case of three-point normal loading symmetric about the x-axis, briefly discussed as an extreme case in Section 4.1.1, was also analysed by SURENDRA and SIMHA [35]. This special case can be derived from Fig. 7 by setting $\beta_1 = 0$, for which coefficients (Eq. (4.7)) of characteristic equation for IP coordinate are given by:

$$A = 1 - 2\cos\beta,\quad B = -5 + 6\cos\beta - \cos 2\beta,\quad G = 4(1 - \cos\beta) + \cos 2\beta \tag{4.12}$$

and the two of the roots can be obtained as:

$$\frac{x_{\mathrm{IP}}}{R} = \frac{3 - 2\cos\beta + \cos 2\beta \pm \sin\beta\sqrt{2(-1 + 4\cos\beta - \cos 2\beta)}}{2(1 - 2\cos\beta)}, \tag{4.13}$$

while the remaining two roots are 1 and 1. Here the only parameter β_2 is replaced by β in the expressions. The first root with '$-$' sign in place of $\pm$ in Eq. (4.13) is real for the whole range of $\beta \in [0°, 90°]$ and it is x-coordinate of the only IP traversing in the disk. The second root with the '$+$' sign there (reciprocal of the first one) is the coordinate of a hypothetical IP.

For the other extreme case of $\beta_1 = 90°$ giving a diametral compression, coefficients of the characteristic equation are: $A = 1$, $B = 4\cos\beta$, $G = 2+\cos 2\beta$ and the two of the roots being: $x_{\mathrm{IP}}/R = -\cos\beta \pm i\sin\beta$, while the other two are equal to the first two. All the roots denote the points on the left half of the circular boundary.

These limiting cases highlight how increasing or reducing symmetry simplifies the stress topology. In particular, diametric compression eliminates interior isotropic points, indicating that the stress field no longer admits isolated zero-shear states within the disk.

4.2. Tangential loading symmetric about an axis

The case of four-point pure tangential loading symmetric about x-axis shown in Fig. 11 is analysed here. Again, β_1 and β_2 are independent parameters varied in this case. Equilibrium of the disk in x-direction leads to: $Q_1 \sin\beta_1 = Q_2 \sin\beta_2$, whereas disk equilibria in y- and θ-directions (moment) are automatically satisfied owing to symmetry.

Similar to the normal loading case in Section 4.1, this problem is solved for the state of stress in the disk as described in Appendix A (Eq. (A.2)) by noting that $P_i = 0$ for all i and $Q_1 = -Q_4$, $Q_3 = -Q_2$. For a given β_1, isochromatic patterns are obtained for various values of $\beta_2 \in [0°, (180° - \beta_1)]$, to generate a video. Three videos corresponding to $\beta_1 = 30°, 45°, 60°$ are made available as supple-

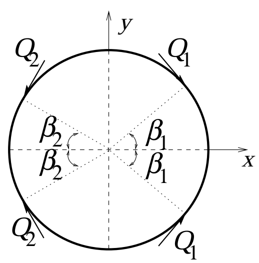

FIG. 11. Circular disk under four-point tangential loading symmetric about the x-axis and asymmetric about the y-axis.

mentary material, and a typical plot is presented in Fig. 12. The magnitude of reference load used for generating patterns using MATLAB is: $Q_1 = 790$ N. Extreme case of $\beta_1 = 0°$ implies a null state of stress (zero loading) as $Q_2 = 0$ and symmetric pair of Q_1 gets self-cancelled. Similarly, $\beta_2 = 0°$ also represents a zero loading.

From all the videos, an IP is observed at the disk centre consistently for all values of input parameters, which is a contrasting feature of tangential loading. This feature observed in simulations can be verified by substituting origin coordinates $r = 0$ into the stress tensor solution. The resulting stress tensor evaluated at origin is:

$$[\sigma]^{4\mathrm{T}}(r=0) = \begin{bmatrix} 0 & 0 \\ 0 & 0 \end{bmatrix}, \tag{4.14}$$

which is a null state of stress independent of any parameters involved. When localised, this is a hydrostatic state that gives rise to IP which is termed as a *singular point* as a special case of IP. Singular points can be found at unloaded protruding corners, at certain boundary points of the circular ring under diametric compression in which they do not play a role in the force transmission within the solid. The central isotropic point corresponding to null stress state represents physically a singular hydrostatic point and distinguishes tangential loading fundamentally from normal loading.

In a typical video for the case of constant β_1, the evolution and motion of IPs can be divided into three regimes. In the first regime starting at $\beta_2 = 0°$, an IP evolves from the left end traverses on the x-axis towards the central immovable IP. When $\beta_2 \approx (90° - \beta_1)$, the second regime begins in which the IP on the x-axis elongates to become a curve of ZOF. In the third regime, the ZOF curve precipitates to 3 IPs: one retained on the x-axis, the other two form in disk quadrants symmetric about the x-axis. The latter two IPs traverses in symmetric curved paths to reach the right-side load points when $\beta_2 = (180° - \beta_1)$ (end of the third regime) while the IP retained on the x-axis continues to traverse within the disk up to some distance. The IP traversing on the x-axis (before or after splitting) has to pass through the central IP in one of these regimes, at which it appears to be merging with central IP and re-evolving from there. If this happens well within the first regime (i.e., when $\beta_1 \ll 45°$) or in the third regime (i.e., when $\beta_1 \gg 45°$), we can clearly see the merging on the left side and re-evolving from the right side. When β_1 is around 45°, we see the blending of different IPs with the central IP. Unlike the normal loading case, where IP coalescence occurs rather abruptly, the evolution here proceeds through an intermediate ZOF region. This indicates a smoother redistribution of zero-shear regions, where they expand and contract continuously rather than merging as discrete entities.

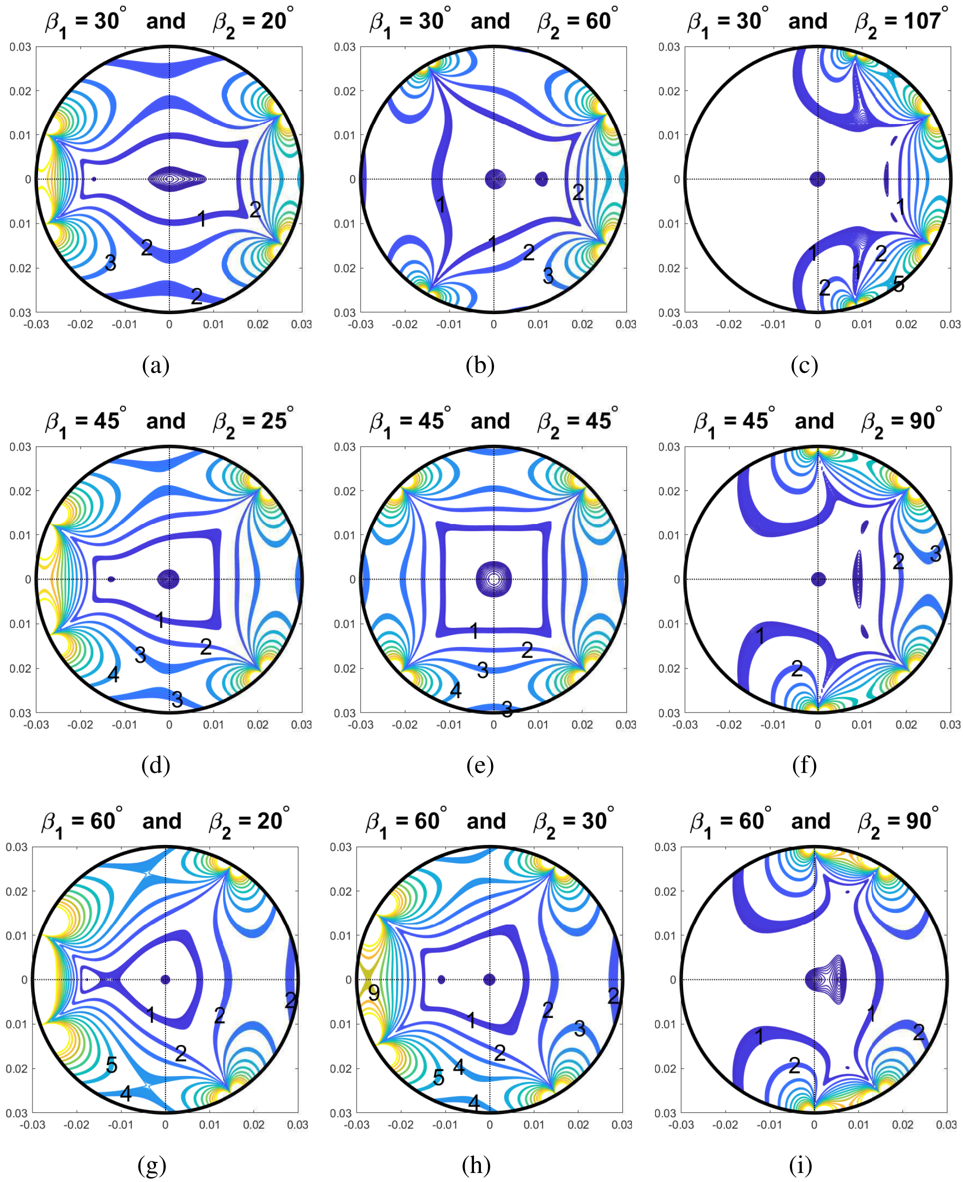

FIG. 12. Simulated isochromatic patterns in circular disk under four-point tangential loading symmetric about x-axis for various combinations of β_1 and β_2. Fringe order (N) values are marked in each pattern. (a), (b), (c): Video4_Cir4TxAxis_Be1is30.mpg; (d), (e), (f): Video5_Cir4TxAxis_Be1is45.mpg; (g), (h), (i): Video6_Cir4TxAxis_Be1is30.mpg.

In Fig. 12, the first column shows the isochromatic fringe contours from the first regime corresponding to $\beta_1 = 30°$, $45°$, $60°$ cases, and the second column shows nearly the beginning of the second regime, and the third column has the contours of the third regime patterns. Unlike the normal loading case, IPs coalescence is not found in this case whereas splitting of an IP on a symmetry axis into two IPs in the quadrants can be observed for both types of loading. However, splitting occurs in the case of tangential loading rather gradually through ZOF formation as an intermediary. The splitting of IPs via the intermediate ZOF can therefore be interpreted as a gradual localisation of regions of near-zero shear stress.

4.2.1. Note on the characteristic equation. The characteristic equation for the pure tangential loading symmetric about only x-axis can be derived in a similar manner to the normal loading as:

$$\left(\frac{x_{\mathrm{IP}}}{R}\right)\left[\left(\frac{x_{\mathrm{IP}}}{R}\right)^5 - K\left(\frac{x_{\mathrm{IP}}}{R}\right)^4 - 2\left(\frac{x_{\mathrm{IP}}}{R}\right)^3 + 4K\left(\frac{x_{\mathrm{IP}}}{R}\right)^2 + (4\cos\beta_1\cos\beta_2 - 3)\left(\frac{x_{\mathrm{IP}}}{R}\right) + K\right] = 0, \tag{4.15}$$

where $K = (\cos\beta_1 - \cos\beta_2)$, which is valid for IPs forming on the x-axis. Equation (4.15) captures the distinct feature of the permanent central IP. Reducing Eq. (4.15) by keeping away the root $x_{\mathrm{IP}} = 0$, it gives a *quintic* (5^{th} degree polynomial) equation for which general solution for arbitrary coefficients is not available using current mathematical techniques [38]. However, for this, a numerical solution could be obtained in the future.

4.2.2. IPs in bi-symmetric tangential loading. As a special case of tangential loading, we consider the four-point loading symmetric about x- and y-axes, as shown in Fig. 13. In this special case, $\beta_1 = \beta_2 = \beta$ is the only parameter and the

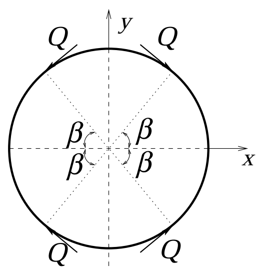

FIG. 13. Circular disk under four-point tangential loading symmetric about both x- and y-axes.

load magnitudes $Q_1 = Q_2 = Q$ while their directions are such that they keep the disk in equilibrium.

Isochromatic patterns are obtained by varying $\beta \in [0°, 90°]$ and animated into Video7 and a snapshot shown in Fig. 14. From the simulations, apart from central IP, a pair of IPs form on the axes of symmetry. The symmetric pair of IPs traverses on the x-axis when $\beta \in [0°, 30°)$ and on y-axis when $\beta \in (60°, 90°]$. When $\beta \in [30°, 60°]$, the pair is embedded into the central IP. These are also verified by plotting the individual stress components along x- and y-axes for different β values to confirm whether $\tau_{r\theta} = 0$ on the entire axis, and to manually find IPs where $\sigma_{rr} = \sigma_{\theta\theta}$. The plots are not shown here for brevity.

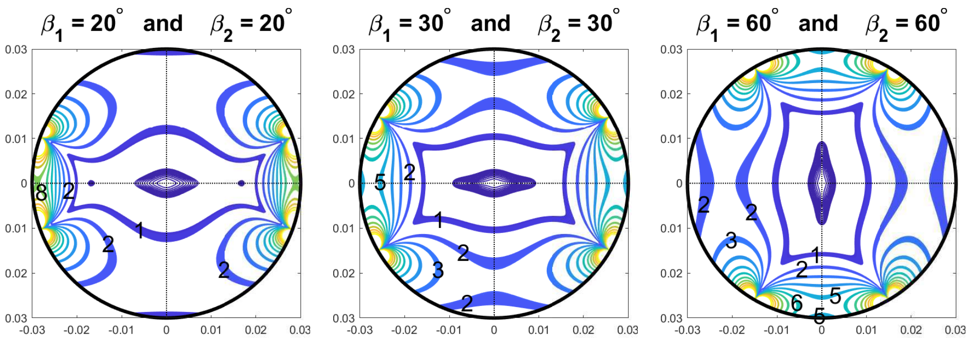

(a) (b) (c)

FIG. 14. Simulated isochromatic patterns in circular disk under four-point bi-symmetric tangential loading for different β. Fringe order (N) values are marked in each pattern. Video7_Cir4TxAxis_Be1isBe2.mpg.

The characteristic equation for the IP coordinates on the x-axis for this bi-symmetric loading case can be derived as:

$$\left(\frac{x_{\mathrm{IP}}}{R}\right)^2 \left[\left(\frac{x_{\mathrm{IP}}}{R}\right)^4 - 2\left(\frac{x_{\mathrm{IP}}}{R}\right)^2 + 2\cos 2\beta - 1\right] = 0, \tag{4.16}$$

for which, the six roots are: $x_{\mathrm{IP}} = 0,\ 0$, $x_{\mathrm{IP}}/R = \pm\sqrt{1 - 2\sin\beta}$ and $x_{\mathrm{IP}}/R = \pm\sqrt{1 + 2\sin\beta}$. The third and fourth roots are the normalized x-coordinates of IP pair when they form on the x-axis thus valid only when $\beta \in [0°, 30°]$. The last roots are about hypothetical IPs. The characteristic equation for IP coordinates on the y-axis can be derived in a similar manner as:

$$\left(\frac{y_{\mathrm{IP}}}{R}\right)^2 \left[\left(\frac{y_{\mathrm{IP}}}{R}\right)^4 - 2\left(\frac{y_{\mathrm{IP}}}{R}\right)^2 - 2\cos 2\beta - 1\right] = 0, \tag{4.17}$$

for which the six roots are: $y_{\text{IP}} = 0, 0$, $y_{\text{IP}}/R = \pm\sqrt{1 - 2\cos\beta}$ and $y_{\text{IP}}/R = \pm\sqrt{1 + 2\cos\beta}$. Again, the middle two roots are the normalized y-coordinates of IP pair valid when $\beta \in [60°, 90°]$.

The coexistence of a central IP with axis-aligned IP pairs reflects the combined influence of symmetry constraints and the intrinsic null-stress condition induced by tangential loading.

4.3. Symmetric oblique loading

Oblique loading can be interpreted as a superposition of normal and tangential loading effects, and therefore exhibits a hybrid behaviour combining axis-constrained IP evolution with centralisation tendencies associated with tangential loading.

Four-point oblique loading on the disk symmetric about only x-axis involves three parameters: load angles β_1, β_2 and load ratio P/Q, whereas its special case of bi-symmetric loading shown in Fig. 15 involves two parameters: $\beta_1 = \beta_2 = \beta$ and P/Q. The latter loading is considered here for a better understanding of the behaviour of IPs under oblique loading.

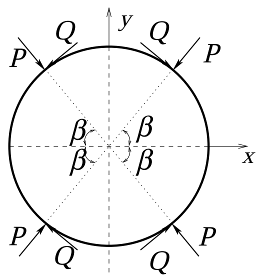

FIG. 15. Circular disk under four-point oblique loading symmetric about x- and y-axes.

A video is generated from the isochromatic patterns of this loading case by varying $\beta \in [0°, 90°]$ for $P = Q$ case, as well as a snapshot as shown in Fig. 16. Similarly, the videos for various other ratios of $P/Q = 0.1, 0.2, \ldots, 0.9$ were also studied, although not presented here. From all those videos, we observed that IPs always form on the symmetry axes for any combination of β and P/Q values. As β increases from zero, two IPs emanate from the ends of the horizontal diameter and traverse on it towards the origin, while the ZOF from the top and bottom portions of the boundary gradually precipitates to two IPs while traversing on the y-axis towards the origin. The two IPs so formed on the y-axis expand back to ZOF and precipitate to IPs again in a short range of β while continuing their motion towards the origin. The two IPs on the x-axis coalesce at the origin when $\beta = 45°$ for any value of P/Q, which is surprising. After the coalescence, they split into two IPs traversing on the y-axis away from each other, and merge with the IPs coming towards origin after two cycles of transformation between ZOF and IPs. All of them disappear immediately after merging. Thus, in a broad sense, there are four IPs in the first regime and no IPs thereafter.

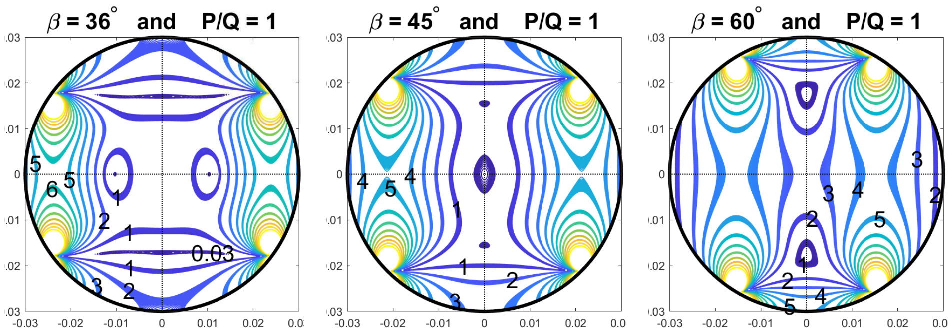

(a) (b) (c)

FIG. 16. Simulated isochromatic patterns in circular disk under four-point bi-symmetric oblique loading for different β given $P = Q$. Fringe order (N) values are marked in each pattern. Video8_Cir4N4TbiSym_PisQ.mpg.

As P increases relative to Q, the transformation cycles between ZOF and IPs would be slower and confined to smaller regions close to the top and bottom boundary regions. The characteristic equation for IPs forming on the x-axis in disk under 4-point bi-symmetric oblique loading (symmetric about x- and y-axes) can be written as the following bi-cubic equation:

$$\begin{aligned}(4.18)\qquad &\left(\frac{P}{Q}\cos 2\beta - \sin 2\beta\right)\left(\frac{x_{\mathrm{IP}}}{R}\right)^6 \\ &+ \left(-2\frac{P}{Q} - \frac{P}{Q}\cos 2\beta + \sin 2\beta\right)\left(\frac{x_{\mathrm{IP}}}{R}\right)^4 \\ &+ \left(2\frac{P}{Q} + \frac{P}{Q}\cos 2\beta + \sin 2\beta - \sin 4\beta\right)\left(\frac{x_{\mathrm{IP}}}{R}\right)^2 - \frac{P}{Q}\cos 2\beta = 0,\end{aligned}$$

for which the three pairs of roots come out to be unwieldy, thus not given here.

4.4. Asymmetric normal loading

If we change the magnitude of a pair of opposite forces in the circular disk under four-point bi-symmetric normal loading, then the symmetry about both the axes gets eliminated, as shown in Fig. 17(a). However, it exhibits 180° rotational symmetry. It can also be perceived as two diametral compressions on the disk rotated from each other by 2β.

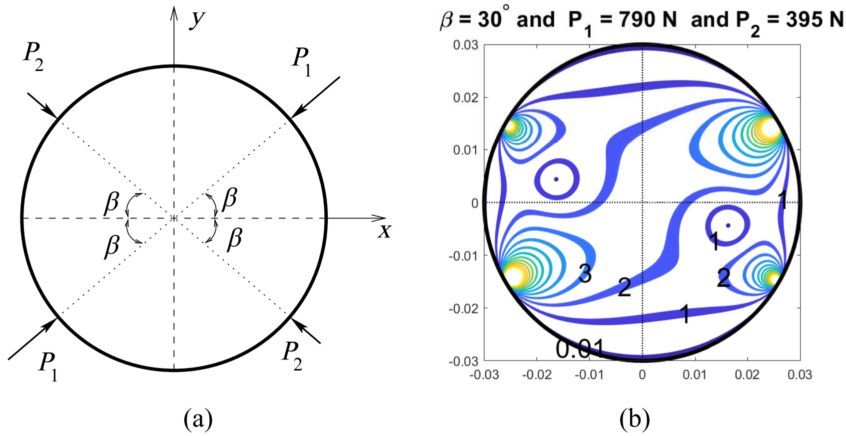

Fig. 17. (a) Circular disk under four-point normal loading with 180° rotational symmetry; (b) isochromatics pattern for typical case. Video9_Cir2dia_180degSym_Be30.mpg.

In the absence of symmetry, zero-shear loci are no longer aligned with principal directions, resulting in isotropic points tracing curved trajectories within the disk. These paths reflect the redistribution of stress between competing load components and can be interpreted as indicative of load transfer pathways.

Isochromatic patterns are generated for the sequences of $P_2/P_1 = 0, 0.01, 0.02, \ldots, 0.99, 1$ and $P_2/P_1 = 1/0.99, 1/0.98, \ldots, 1/0.01$ for $\beta = 30°$ and animated into a video as well as the snapshot as shown in Fig. 17(b). Two IPs are found throughout the range of P_2/P_1 forming diametrically opposite to each other with 180° symmetry of the problem. When $P_2/P_1 = 0$, the IP pair emanates from the boundary at P_2 load points, traverses in a symmetric pair of curved paths inside the disk region in an opposite sense to reach the P_1 load points on the boundary when $P_2/P_1 \to \infty$ or $P_1 = 0$. The pair forms on the x-axis when $P_2 = P_1$ which is a bi-symmetric case. A similar trend is observed with few other values of $\beta < 45°$. The curved paths resemble hyperbola whose principal axes are x- and y-axes. For $\beta = 45°$ case which is another bi-symmetric loading, the IP pair traverses on the two perpendicular diameters connecting the load points on the boundary, i.e., they traverse on 'X' shaped straight paths coalescing and diverting at the origin. $\beta > 45°$ cases are 90° rotated versions of $\beta < 45°$ cases, thus $\beta = 45°$ is like a mirror image between the two sub-ranges. Since we could not identify an axis of symmetry for this loading condition, we did not derive a single characteristic equation. There are two non-linear equations in two unknown coordinates of IPs, and hence a closed-form solution is seldom possible. Thus, this can be approached using a numerical method to get the precise coordinates of IPs in such cases in the future.

4.5. Unified physical interpretation of fringe patterns

The diverse fringe patterns observed across all loading configurations can be interpreted within a unified physical framework governed by fundamental principles. First, isotropic points correspond to zero-shear locations and therefore lie on zero-shear loci of the stress field. Second, symmetry plays a dominant role in constraining these loci to specific directions, leading to axis-confined IPs. Third, the coalescence of IPs represents a transition in stress topology associated with the merging of zero-shear regions. Fourth, tangential loading introduces a persistent central null-stress point, fundamentally altering the structure of the stress field. Finally, while the magnitude of loading does not influence IP positions, their locations are highly sensitive to loading directions, making them robust indicators of loading configuration. All the loading cases presented in this section can therefore be interpreted as manifestations of these underlying principles. This framework enables the interpretation of complex fringe patterns without recourse to case-specific analysis, thereby providing a generalised understanding of IP behaviour in photoelastic systems.

5. Determination of experimental loads

The physical interpretation developed in Section 4 provides the basis for solving the inverse problem. Since isotropic points correspond to zero-shear loci that depend on load orientation, their coordinates encode information about the underlying contact forces.

To quantify the four oblique loads (each resolved into normal and tangential components) asymmetrically acting on a circular disk in the experiment shown in Fig. 5, we make use of the framework developed in Section 4. Here, the coordinates of the two IPs are known from the digital image analysis of the experimental isochromatics, provided in Section 2.4. We have to find the oblique loads acting at the four points on the boundary causing the IPs to form there. This is an inverse problem while those considered in Section 4 are forward problems.

If we substitute polar coordinates of one IP along with experimental load angles (β_i^{exp} values quantified in Section 2.4) into Eq. (4.3), we get two independent linear equations in terms of unknown load components P_i^{exp} and Q_i^{exp} for $i = 1, 2, 3, 4$. Using the other IP coordinates in the same Eqs. (4.3), we can get two more equations in terms of the same unknowns. These four equations together with three equations are provided by Eqs. (3.1) and the applied load transfer given by Eq. (3.2), can be solved for the 8 unknown load components.

By substituting experimental β_i values into Eqs. (3.1) and (3.2) and truncating the coefficients after 6^{th} decimal or 6 significant digits, we get the following four linear equations for Q_i^{exp} in terms of P_i^{exp} all of which are unknown at this stage,

$$\begin{Bmatrix} Q_1 \\ Q_2 \\ Q_3 \\ Q_4 \end{Bmatrix}^{\exp} = \begin{bmatrix} 0.527 & 0.834 & 0.224 & -0.224 \\ -0.899 & -0.462 & 0.156 & -0.156 \\ 0.187 & -0.187 & 0.459 & 0.837 \\ 0.185 & -0.185 & 0.840 & -0.457 \end{bmatrix} \begin{Bmatrix} P_1 \\ P_2 \\ P_3 \\ P_4 \end{Bmatrix}^{\exp} + \begin{Bmatrix} -636.023 \\ 698.69 \\ -678.171 \\ 615.504 \end{Bmatrix}. \tag{5.1}$$

Substitution of $(r_{\mathrm{IP1}}, \theta_{\mathrm{IP1}})$ into Eqs. (4.3) and that of $(r_{\mathrm{IP2}}, \theta_{\mathrm{IP2}})$ into the same Eqs. (4.3) can be represented as:

$$\begin{aligned} &\sigma_{rr}^{\mathrm{4N4T}}(r_{\mathrm{IP1}}, \theta_{\mathrm{IP1}}) = \sigma_{\theta\theta}^{\mathrm{4N4T}}(r_{\mathrm{IP1}}, \theta_{\mathrm{IP1}}), \\ &\tau_{r\theta}^{\mathrm{4N4T}}(r_{\mathrm{IP1}}, \theta_{\mathrm{IP1}}) = 0, \\ &\sigma_{rr}^{\mathrm{4N4T}}(r_{\mathrm{IP2}}, \theta_{\mathrm{IP2}}) = \sigma_{\theta\theta}^{\mathrm{4N4T}}(r_{\mathrm{IP2}}, \theta_{\mathrm{IP2}}), \\ &\tau_{r\theta}^{\mathrm{4N4T}}(r_{\mathrm{IP2}}, \theta_{\mathrm{IP2}}) = 0, \end{aligned} \tag{5.2}$$

where the polar coordinate stress components with the superscript '4N4T' are the components of the resulting stress tensor in Eq. (4.1) after superposing the nine states of stress on its RHS. Further, by substituting experimental β_i values, IP coordinates and $R = 0.03$ m, $h = 0.006$ m, $P = 790$ N into Eq. (5.2) and using Eq. (5.1), we get the following four equations in terms of $P_i^{\exp}$ only, after keeping 6 significant digits,

$$\begin{bmatrix} 3942.07 & -1395.75 & 598.608 & -2760.23 \\ 2760.23 & -2449.29 & 1329.07 & -889.81 \\ -1256.18 & -1165.43 & 2935.08 & 1649 \\ 1340.92 & -1405.37 & 2935.08 & -2031.13 \end{bmatrix} \begin{Bmatrix} P_1^{\exp} \\ P_2^{\exp} \\ P_3^{\exp} \\ P_4^{\exp} \end{Bmatrix} = \begin{Bmatrix} 760334 \\ -476541 \\ 1.066 \times 10^6 \\ 54056.2 \end{Bmatrix} \tag{5.3}$$

upon solving which, we find the experimentally prevailing radial load components on the circular disk as:

$$\begin{aligned} P_1^{\exp} &= 568.517 \text{ N}, \quad & P_2^{\exp} &= 352.682 \text{ N}, \\ P_3^{\exp} &= 486.073 \text{ N}, \quad & P_4^{\exp} &= 463.553 \text{ N}. \end{aligned} \tag{5.4}$$

Using these normal load values in Eq. (5.1), we evaluate the experimentally prevailing tangential load components on the circular disk as:

$$\begin{aligned} Q_1^{\exp} &= -37.086 \text{ N}, \quad & Q_2^{\exp} &= 28.009 \text{ N}, \\ Q_3^{\exp} &= -26.601 \text{ N}, \quad & Q_4^{\exp} &= 35.679 \text{ N}. \end{aligned} \tag{5.5}$$

Positive values for all the normal loads indicate that they are all compressive, as per the convention adopted in the formulation. Referring to Fig. 5, $P_1^{\exp} = 568.517$ N is the largest normal load which is acting at the topmost point of the disk among other normal loads. $P_2^{\exp} = 352.682$ N is the least among all normal loads, which is acting at the top left side of the disk. The last two observations indicate that P_1^{exp} has significantly more role in transferring the applied vertical load down to the supports. There is only a minor difference between the values of P_3^{exp} and P_4^{exp} values, indicating almost an equal contribution from the bottom supports. The observations of higher fringe concentration at β_1^{exp} boundary point in Fig. 5 than at β_2^{exp} point and almost equal fringe concentrations at β_3^{exp} and β_4^{exp} points support our conclusions.

A positive value for a tangential load indicates that it causes CCW moment at the disk centre, by convention. Thus, negative values for Q_1^{exp} and Q_3^{exp} indicate that they cause CW moment whereas the other two Q_i^{exp} cause the CCW moment at disk centre. Magnitudes of Q_i^{exp} are less than their corresponding P_i^{exp} by nearly 15 times. The angle of friction at the four contacts can be found as:

$$\begin{aligned}
\gamma_1^{\text{exp}} &= \arctan \frac{Q_1^{\text{exp}}}{P_1^{\text{exp}}} = -\arctan(0.065) = -3.7^\circ,\\
\gamma_2^{\text{exp}} &= \arctan \frac{Q_2^{\text{exp}}}{P_2^{\text{exp}}} = \arctan(0.079) = 4.5^\circ,\\
\gamma_3^{\text{exp}} &= \arctan \frac{Q_3^{\text{exp}}}{P_3^{\text{exp}}} = -\arctan(0.055) = -3.1^\circ,\\
\gamma_4^{\text{exp}} &= \arctan \frac{Q_4^{\text{exp}}}{P_4^{\text{exp}}} = \arctan(0.077) = 4.4^\circ.
\end{aligned} \tag{5.6}$$

In Eq. (5.6), all the numbers are static friction angles (or coefficients of static friction) which are very small here, thus indicating a low tendency for relative motion between loading/supporting bars and the disk specimen in the experimental configuration considered here. Negative value for Q_1^{exp} indicates that the resultant load is more vertical than otherwise at β_1^{exp} boundary point making the local fringes (at P_1 or Q_1) are aligned more vertically rather than radially. A positive value for Q_4^{exp} indicates that the resultant load is again more vertical than otherwise at β_4^{exp} point. The last two predictions imply that the fringes around the two loading points at the right side resemble the fringe distribution in the diametrically compressed disk. Similar predictions can be made about the left side loading points. All these conclusions can be verified with Fig. 5, which is reproduced here in Fig. 18(a) for direct comparison against the simulated isochromatic pattern using the experimentally prevailing loads.

From Fig. 18 we observe that the simulated fringe patterns match closely with the experiments including capturing the essential features such as '8' shaped first order fringe around IPs, slight tilting of fringes near the load points at the boundary, and the weak and strong fringe concentrations at β_2^{exp} and β_1^{exp} points, respectively. This matching of patterns validates the normal and tangential load values determined, and the generic analytical approach proposed above.

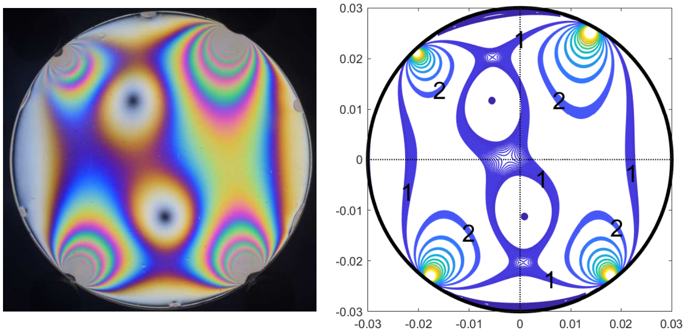

(a) (b)

FIG. 18. Simulated isochromatic pattern using experimental loads: (a) experimental result, (b) analytical prediction (the values of fringe order N are marked).

It is important to note that the inverse methodology presented here assumes that contact force directions (β_i) remain constant during loading. While this assumption is appropriate for the controlled experimental configuration considered in this study, it may not directly hold in more complex industrial systems where contact orientations can evolve dynamically due to deformation, frictional slip, or multi-body interactions. Therefore, the present formulation should be viewed as a foundational framework, most applicable to systems with well-defined or constrained contact geometries. Extension of this approach to more general industrial applications will require coupled modelling of contact kinematics and may involve additional measurement or estimation strategies for determining load directions.

For extending this method to any other 2-D solid geometry under a prescribed loading configuration, we should know the analytical solution for distribution of stresses in the solid. Then the demonstrated method can be applied directly using the information of IPs formed. In case of numerical solution to the problem of interest, one may employ curve-fitting (surface-fitting for 2-D domains) techniques to express the stress distributions as functions of domain coordinates (x, y or r, θ). Reliable expressions for stress components applicable for the problem can ensure enough accurate contact friction values found.

6. Conclusions

This study investigated the formation, evolution, and practical utility of isotropic points (IPs) in circular disks subjected to multi-point loading using analytical modelling and photoelastic experiments. While multiple loading configurations were analysed, the results show that the observed fringe patterns and IP behaviour can be understood through a unified physical framework.

First, it is established that isotropic points correspond to zero-shear locations in the stress field and therefore lie on zero-shear loci. The structure of these loci is governed primarily by the symmetry of loading. When symmetry is present, IPs are confined to symmetry axes, whereas symmetry breaking leads to their migration into the interior of the disk along curved trajectories. These trajectories reflect the redistribution of stress and can be interpreted as indicative of load transfer pathways. Second, the evolution of IPs is characterised by mechanisms of formation, coalescence, and splitting. In normal loading cases, pairs of IPs form along symmetry axes, merge at critical parameter values, and subsequently migrate into the domain. This coalescence represents a transition in the topology of the stress field associated with the merging of zero-shear regions. Third, tangential loading produces qualitatively different behaviour by introducing a persistent central isotropic point corresponding to a null stress state. Unlike normal loading, where coalescence occurs abruptly, the evolution of IPs in tangential loading proceeds through intermediate zeroth-order fringe (ZOF) regions, indicating a smoother redistribution of zero-shear zones. Fourth, it is demonstrated that the locations of IPs are independent of the load magnitude but highly sensitive to the load direction and orientation. This invariance makes IPs robust markers for characterising loading geometry and enables their use in inverse analysis.

The inverse approach developed enables the determination of normal and tangential contact load components directly from the experimentally measured coordinates of IPs. The good agreement between simulated and experimental fringe fields validates the approach and highlights the capability of IP-based analysis for non-invasive load identification. Overall, the study demonstrates that the diverse fringe patterns observed under different loading configurations can be interpreted within a unified framework governed by symmetry, stress topology, and load orientation. This provides a deeper physical understanding of photoelastic phenomena and strengthens the role of isotropic points as fundamental descriptors in stress analysis.

Building on the current findings, future research could explore the behaviour of isotropic points in functionally graded materials (FGMs), which exhibit spatially varying properties [39]. This will involve adapting the analytical framework to account for material gradients and validating the results through advanced photoelastic experiments. Additionally, the methodology can be extended to three-dimensional geometries and dynamic loading conditions to better simulate real-world applications. Investigating IP behaviour in composite structures and under thermal loads will further enhance the applicability of this work in aerospace, biomedical, and civil engineering domains.

Appendix A: Method to solve circular disk problems

This appendix describes a general method for determining the state of stress in a circular disk subjected to the action of any number of concentrated loads. The loads can have normal and tangential components acting at discrete points on the periphery only. This method relies on the superposition principle [15, 35]. The following description summarizes the method. The classical problem of a semi-infinite plate with a concentrated load at the straight boundary (half-plane) shown in Fig. 19(a) is solved by Flamant by an analogy from hydrostatics, leading to radial stress distribution [9]. Such half-plane geometry is assumed tangential to the periphery of a circular disk at a point of loading with disk domain comprising half-plane and the point loads coincided. Half-planes required for idealising the contacts of the disk problem are as many as the point loads acting on the disk. All the half-plane solutions are linearly superposed after expressing them with respect to a consistent global coordinate system at the disk centre. The half-plane required for a typical point load is shown in Fig. 19(b) along with the central global coordinate system. The required solution is obtained by superposing a hydrostatic stress state for correcting the boundary traction.

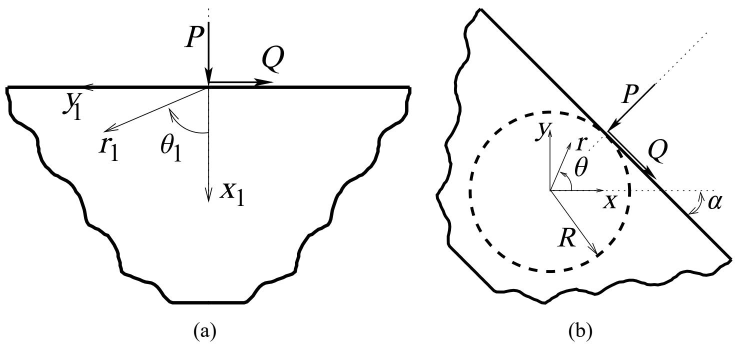

Fig. 19. Flamant problem with both normal and tangential load components with respect to (a) local left-handed coordinate system, (b) global right-handed coordinate system.

The state of stress contributed by a concentrated load acting at $\theta = (90° - \alpha)$ on the disk periphery, shown in Fig. 19(b), is given [35] by:

$$
\text{(A.1)}\qquad [\sigma]^{\mathrm{GenFl}} = \begin{bmatrix} \sigma_{rr} & \tau_{r\theta} \\ \tau_{r\theta} & \sigma_{\theta\theta} \end{bmatrix}^{\mathrm{GenFl}} = \frac{-2P}{\pi h} \frac{\{R\cos\gamma - r\sin(\alpha - \gamma + \theta)\}}{\{r^2 + R^2 - 2rR\sin(\alpha + \theta)\}^2} \times \begin{bmatrix} \{r - R\sin(\alpha+\theta)\}^2 & -\mathrm{Sym}- \\ -R\cos(\alpha+\theta)\{r - R\sin(\alpha+\theta)\} & R^2\cos^2(\alpha+\theta) \end{bmatrix}.
$$

The state of stress due to the combined action of n point loads of magnitudes $P_1, P_2, \ldots, P_n$ acting into the disk inclined to radial direction by $\gamma_1, \gamma_2, \ldots, \gamma_n$

measured CCW acting at $\theta = \theta_1, \theta_2, \ldots, \theta_n$ on the periphery, respectively, can be written as:

$$[\sigma] = \sum_{i=1}^{n} [\sigma]^{\mathrm{GenFl}}(P = P_i,\, \gamma = \gamma_i,\, \alpha = 90^\circ - \theta_i) + \frac{\sum_{i=1}^{n} P_i \cos\gamma_i}{2\pi R h} \begin{bmatrix} 1 & 0 \\ 0 & 1 \end{bmatrix}, \tag{A.2}$$

in which the parentheses after the stress tensor for the generalized Flamant problem indicate substitution of the parameters. The last term of the above equation is the hydrostatic stress to get the traction-free boundary, excluding the loaded points.

Acknowledgements

The authors would like to thank Prof. K.R.Y. Simha, Indian Institute of Science (IISc), Bangalore for allowing us to use the photoelasticity lab for conducting the experiments presented here.

Ethical considerations.

Ethical approval was not required.

Declaration of conflicting interest

The author(s) declared no potential conflicts of interest with respect to the research, authorship, and/or publication of this article.

Supplementary materials

Supplementary materials, including videos and an m-file with a MATLAB program, are available along with this article: https://doi.org/10.24423/aom.4846.sm.

References

1. L.L. Howell, *Compliant Mechanisms*, John Wiley & Sons, New York, 2001.
2. B. Zhu, X. Zhang, H. Zhang, J. Liang, H. Zang, H. Li, R. Wang, *Design of compliant mechanisms using continuum topology optimization: A review*, Mechanism and Machine Theory, **143**, 103622, 2020.
3. O. Tsoungui, D. Vallet, J.C. Charmet, *Numerical model of crushing of grains inside two-dimensional granular materials*, Powder Technology, **105**, 190–198, 1999.
4. S.J. Antony, *Link between single-particle properties and macroscopic properties in particulate assemblies: role of structures within structures*, Philosophical Transcreations of the Royal Society A: Mathematical, Physical and Engineering Sciences, **365**, 2879–2891, 2007.

5. A. Hassanpour, C.C. Kwan, B.H. Ng, N. Rahmanian, Y.L. Ding, S.J. Antony, X.D. Jia, M. Ghadiri, *Effect of granulation scale-up on the structure and strength of granules*, Powder Technology, **189**, 2, 304–312, 2009.

6. J.W. Dally, W.F. Riley, *Experimental Stress Analysis*, McGraw Hill, Singapore, 1987.

7. E.G. Coker, L.N.G. Filon, *A Treatise on Photo-elasticity*, Cambridge University Press, Cambridge, 1957.

8. M.M. Frocht, *Photoelasticity*, Vol. 1, John Wiley & Sons, New York, 1941.

9. S.P. Timoshenko, J.N. Goodier, *Theory of Elasticity*, 3rd ed., McGraw-Hill, Singapore, 1970.

10. A. Kuske, G. Robertson, *Photoelastic Stress Analysis*, John Wiley & Sons, London, 1974.

11. H.J. Hutchinson, J.F. Nye, P.S. Salmon, *The classification of isotropic points in stress fields*, *Journal of Structural Mechanics*, **11**, 371–381, 1983.

12. A.J. Durelli, A. Shukla, *Analysis of photoelastic fringes in wave propagation problems*, Journal of Applied Mechanics, **50**, 460–462, 1983.

13. K. Ramesh, *Digital Photoelasticity – Advanced Techniques and Applications*, Springer-Verlag, Berlin, 2000.

14. K. Ramesh, B.R. Pramod, *Digital image processing of fringe patterns in photomechanics*, Optical Engineering, **31**, 86–92, 1992.

15. K.V.N. Surendra, K.R.Y. Simha, *Digital image analysis around isotropic points for photoelastic pattern recognition*, Optical Engineering, **54**, 081209, 2015.

16. Y. Uemura, M. Takai, K. Takemura, *Measurement of the coefficient of friction by the photo-elastic method (I)*, Kyoto University, 42, 1950.

17. Y. Uemura, M. Takai, *Measurement of the coefficient of friction by the photo-elastic method (II)*, Kyoto University, 50–51, 1952.

18. I.M. Fedorchenko, R.A. Kovynev, V.A. Makovetskii, L.L. Sitnikov, *A photoelastic technique for examining contact stresses in powder compaction*, Soviet Powder Metallurgy and Metal Ceramics, **71**, 850–854, 1968.

19. M. Comninou, *Stress singularity at a sharp edge in contact problems with friction*, Zeitschrift für Angewandte Mathematik und Physik, **27**, 493–499, 1976.

20. A. Shukla, H. Nigam, *A numerical-experimental analysis of the contact stress problem*, Journal of Strain Analysis for Engineering Design, **20**, 241–245, 1985.

21. M.P. Hariprasad, K. Ramesh, *Analysis of contact zones from whole field isochromatics using reflection photoelasticity*, Optics and Lasers in Engineering, **105**, 86–92, 2018.

22. M.S.-B. Fernández, *Metrological considerations in the measurement of contact stress parameters using photoelasticity*, Optics and Lasers in Engineering, **117**, 29–39, 2019.

23. R.J. Sanford, J.W. Dally, *A general method for determining mixed-mode stress intensity factors from isochromatic fringe patterns*, Engineering Fracture Mechanics, **11**, 621–633, 1979.

24. S. Barbat, R. Rao, *Photoelastic investigation of metal-forming processes using new sapphire dies*, Experimental Techniques, **6**, 40–43, 1990.

25. J.W. Dally, Y.M. Chen, *A photoelastic study of friction at multipoint contacts*, Experimental Mechanics, **31**, 144–149, 1991.

26. R.L. Burguete, E.A. Patterson, *A photoelastic study of contact between a cylinder and a half-space*, Experimental Mechanics, **37**, 314–323, 1997.

27. J.H. Nam, J.S. Hawong, S. Han, S. Park, *Contact stress of O-ring under uniform squeeze rate by photoelastic experimental hybrid method*, Journal of Mechanical Science and Technology, **22**, 2337–2349, 2008.

28. D.C. Shin, J.H. Nam, D.W. Kim, *Experimental interior stress fields of a constantly squeezed O-ring modeling from hybrid transmission photoelasticity*, Experimental Techniques, **40**, 59–72, 2016.

29. B. Foust, J. Lesniak, R. Rowlands, *Determining individual stresses throughout a pinned aluminum joint by reflective photoelasticity*, Experimental Mechanics, **51**, 1441–1452, 2011.

30. B.E. Foust, R.E. Rowlands, *Thermoelastic determination of individual stresses in a diametrally loaded disk*, Strain, **47**, 146–153, 2011.

31. S.J. Antony, M. Al-Sharabi, N. Rahmanian, T. Barakat, *Shear stress distribution within narrowly constrained structured grains and granulated powder beds*, Advanced Powder Technology, **26**, 1702–1711, 2015.

32. S.J. Antony, D. Chapman, J. Sujatha, T. Barakat, *Interplay between the inclusions of different sizes and their proximity to the wall boundaries on the nature of their stress distribution within the inclusions inside particulate packing*, Powder Technology, **286**, 98–106, 2015.

33. S.J. Antony, D. Chapman, *Probing shear stress distribution within single particle scale inside particulate packing*, KONA Powder and Particle Journal, **28**, 180–188, 2011.

34. G. Cheng-yao, Q. Jia-fu, Q. Nan-sheng, Z. Guo-chun, Z. Hou-he, Y. Qiao, B. Xiang-dong, W. Chao, *The relationship between the friction coefficient and the asperities original inclination angle*, Research Journal of Applied Sciences, Engineering and Technology, **6**, 11, 1906–1910, 2013.

35. K.V.N. Surendra, K.R.Y. Simha, *Characterizing frictional contact loading via isochromatics*, Experimental Mechanics, **54**, 1011–1030, 2014.

36. K.L. Johnson, *Contact Mechanics*, Cambridge University Press, Cambridge, 1987.

37. V. Ramakrishnan, K. Ramesh, *A novel method for the evaluation of stress-optic coefficient of commercial float glass*, Measurement, **87**, 13–20, 2016.

38. M.I. Rosen, *Niels Hendrik Abel and equations of the fifth degree*, The American Mathematical Monthly, **102**, 495–505, 1995.

39. L. Sondhi, R.K. Sahu, R. Kumar, S. Yadaw, S. Bhowmick, R. Madan, *Functionally graded polar orthotropic rotating disks: Investigating thermo-elastic behavior under different boundary conditions*, International Journal on Interactive Design and Manufacturing, **18**, 159–166, 2024.

Received December 2, 2025; revised version June 6, 2026.

Published online June 24, 2026.